ADVANCED FUNCTIONAL MATERIALS
www.afm-journal.de

Carbon-Doped Boron Nitride Nanosheets with Ferromagnetism above Room Temperature

Chong Zhao, Zhi Xu, Hao Wang, Jiake Wei, Wenlong Wang, Xuedong Bai, and Enge Wang**

The possibility to induce magnetism in light-element materials that contain only s and p electrons is of fundamental and practical importance. Here, weak high-temperature ferromagnetism is observed in carbon-doped boron nitride (B-C-N) nanosheets. The bulk-quantities of B-C-N nanosheets that are free of metallic impurities are prepared through a multi-step process. These B-C-N samples exhibit ferromagnetic hysteresis stable at room temperature and above, with saturation magnetization and coercivity comparable to the previously reported results of defective graphite samples. The ferromagnetic response disappears upon the removal of carbon dopants from the BN lattice, indicating that the observed magnetism originates from substitutional carbon-doping rather than from extrinsic magnetic impurities. On the basis of first-principle calculations it is shown that not only substitutional carbon doping in a honeycomb BN lattice favors spontaneous spin polarization and local moment formation, but also that the spin moments can exhibit long-range magnetic ordering.

1. Introduction

Traditionally the origin of magnetism in solids is associated with transition metal elements containing 3d or 4f electrons. Over the past decade, however, there has been increasing evidence that spontaneous magnetization can also occur in metal-free light-element systems that involve only s and p electrons.[1–13] Importantly, theoretical predictions suggest that materials based on sp-elements have high magnitudes of spin-wave stiffness,[14] such that Stoner ferromagnetism with a relatively high Curie temperature, even above room temperature, can be expected.[15] Novel high temperature magnetic materials and nanostructures made of light elements may offer interesting possibilities for potential device applications in spintronics and quantum information processing.

C. Zhao, H. Wang, Prof. E. Wang
International Center for Quantum Materials
School of Physics, Peking University
Beijing 100871, P. R. China
E-mail: egwang@pku.edu.cn
C. Zhao, Dr. Z. Xu, H. Wang, J. Wei,
Prof. W. Wang, Prof. X. Bai
Beijing National Laboratory for Condensed Matter Physics
Institute of Physics
Chinese Academy of Sciences
Beijing 100190, P. R. China
E-mail: wwl@aphy.iphy.ac.cn

DOI: 10.1002/adfm.201401149

In the context of light-element magnetism, graphene-based sp^2 carbon materials have been the most studied materials to date. Although ideal graphene and graphite are non-magnetic in nature, the presence of point defects (e.g., vacancies[2] and covalent adatoms[9–12]) in graphitic networks may induce spin polarization and lead to the formation of a local magnetic moment. Provided that there exists long-range magnetic coupling between these local moments, collective magnetism will then occur.[2,10–12] For instance, weak high-temperature ferromagnetism has been extensively observed in some defective graphitic structures, such as proton-bombarded highly oriented pyrolytic graphite (HOPG),[2] and covalently functionalized monolayer and/or few-layer graphene.[10–12] Apart from defect-induced magnetism, considerable progress has also been made in studying the edge magnetism in zigzag graphene nanoribbons (GNRs).[13,16] The key to the emergence of edge magnetism are highly localized edge-states that form flat (i.e., dispersionless) bands and give rise to a very high density of electronic states around the Fermi energy.[17] Spontaneous magnetization at the edges could then occur as a consequence of on-site Coulomb repulsion.[17,18]

The light element-based magnetism is, of course, not peculiar to the pure carbon materials. The isostructural hexagonal boron nitride (BN) and the ternary B-C-N systems are also intriguing candidates in this aspect.[19–31] Early in 2001, there has been a theoretical study predicating the existence of magnetic ordering in honeycomb heterosheet consisting of C and BN segments with the zigzag-shape boundary.[23] Later on, a variety of C/BN heterostructures, including nanotubes,[24,25] nanoribbons,[26,27] as well as graphene islands embedded in BN sheet and vice versa,[28,31] have also been theoretically investigated, thereby revealing various scenarios of magnetism. However, it is worth noting that the onset of magnetism in these heterostructures is sensitively dependent on atomic-level control of the geometry and configuration of C/BN interface. Such delicate control in theoretical considerations is very difficult to achieve in reality. An alternative and easier way to induce spin polarization in B-C-N systems is the random substitution of B and/or N atoms in a BN honeycomb lattice with C atoms. As predicted by previous theoretical studies, a substitutional C dopant in a BN nanotube[29] or sheet[30] possesses a net magnetic moment of 1 μ_B independent of substitutional site (B or N). This suggests the possibility of producing B-C-N derived

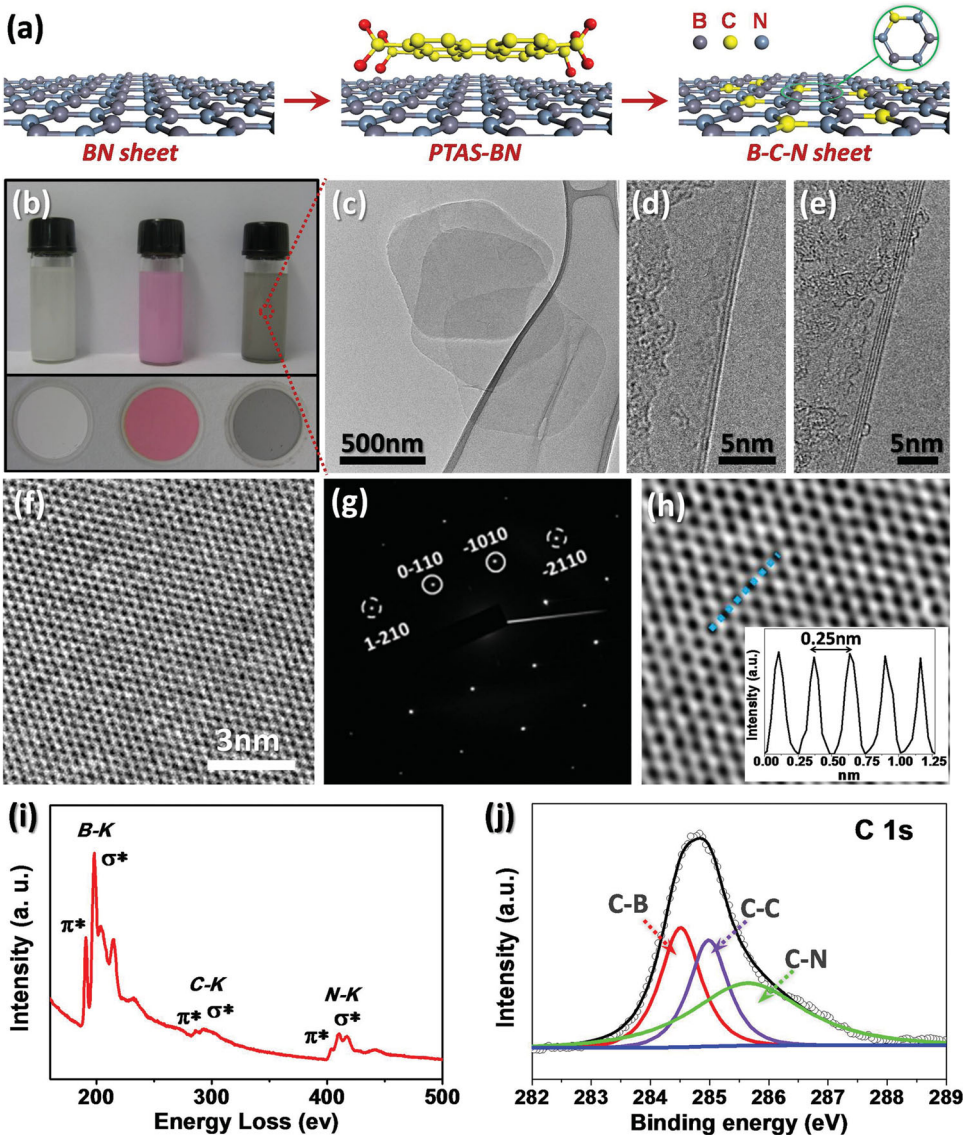

Figure 1. Synthesis and characterization of B-C-N nanosheets. a) Schematic of synthesis of B-C-N nanosheets. b) Photographs of typical dispersions of BN nanosheets in NMP, PTAS functionalized BN nanosheets in aqueous solution, and B-C-N nanosheets in NMP (top, shown left to right). Photographs of corresponding free-standing films (bottom). c) A typical low magnification TEM image of the B-C-N nanosheets. d,e) HRTEM images of the folded edges of several nanosheets with 2, 4 layers respectively. f,g) HRTEM image and associated electron diffraction (ED) pattern revealing typical six-fold symmetry of B-C-N nanosheets. h) Low-pass Wiener filtering of a section of the image in (f). Inset: intensity analysis along the blue dashed line reveals a hexagon width of 0.25 nm. i) Representative EELS spectrum of an individual B-C-N nanosheet. j) XPS spectra of C 1s core levels. The spectrum curves (open circles) are deconvoluted by Gaussian fitting (black solid curves).

magnetic materials through the substitutional C doping of BN nanotubes or nanosheets, but there has been no direct experimental evidence thus far. Herein, we report on the bulk-quantity synthesis of high-quality C doped BN (B-C-N) nanosheets, and the first experimental observations of high-temperature ferromagnetism in such B-C-N based ternary light-element materials.

2. Results and Discussion

The synthesis of B-C-N nanosheets was achieved through a multi-step process. The key procedures that involved the substitutional incorporation of C dopants into the honeycomb lattice of exfoliated BN nanosheets, as illustrated in **Figure 1**a, were essentially the same as previously reported by us for the synthesis of C doped BN nanotubes.[32] The highly exfoliated BN nanosheets, that were prepared by the liquid-phase exfoliation of high-purity BN powders in N-methyl-2-pyrrolidone (NMP),[33] were first nonconvalently functionalized in aqueous solution by π-stacking of an anionic perylene derivative, namely perylene-3,4,9,10-tetracar-boxylic acid tetrapotassium salt (PTAS). Then thermal degradation of the grafted PTAS molecules would lead to the generation of tiny graphitic C species which can be incorporated into BN nanosheets through a slow

C/BN substitution reaction process at an elevated temperature (1373 K). Figure 1b shows the optical photographs of the whole processing sequence in a typical experimental run. Due to their reduced layer-numbers, the exfoliated BN nanosheets can be well-dispersed in NMP (Figure 1b, top). After the non-covalent functionalization by PTAS, the presence of plenty of surface-attached COO^- functional groups imparted a good aqueous solubility to the BN nanosheets (Figure 1b, top). After the final C-doping step, the resultant B-C-N nanosheets were no longer water-soluable but still can be well-dispersed in NMP (Figure 1b, top), just similar to the starting pristine BN nanosheets. Since these three sequence of nanosheets can form stable dispersions in either NMP or in aqueous solution, they can further form good solid films via the vacuum filtration the correponding dispersions aginst a polytetrafluoroethylene (PTFE) membrane (Figure 1b, botttom). This synthetic method can yield bulk quantities of B-C-N nanosheets (typically, tens of mg) that were suitable for SQUID-VSM magnetometry. Note that extreme care must be taken to use highest purity solvents (content of magnetic impurities <1 ppm) so as to avoid any metallic magnetic contamination to the samples.

Figure 1c shows a typical transmission electron microscopy (TEM) image of B-C-N nanosheets with lateral sizes of a few micrometers. Most of the B-C-N nanosheets consisted of a few layers (Figure 1d,e), with the layer number typically in the range of ≈2–5. It has been reported that C atoms substituting for B or N atoms was energetically favorable[29,30,34] and resulted in low distortion in the BN lattice,[35] which was verified by high resolution TEM (HRTEM) results (Figure 1f,h) and associated electron diffraction (ED) patterns (Figure 1g). Figure 1h shows sections of the images in Figure 1f, after low-pass Wiener filtering was performed. Intensity analysis (inset of Figure 1h) along the blue dashed line reveals a hexagon width of 0.25 nm, deducing the spacing between two atoms to be ≈0.143 nm, close to the B-N bond length of 0.144 nm.

The elemental compositions of the as-synthesized B-C-N nanosheets were carefully investigated using electron energy loss spectroscopy (EELS). Figure 1i displayed the core-loss K-edges of B, C, and N located at 188, 284, and 401 eV, respectively. The sharply defined 1s → π^* and 1s → δ^* transition features of the B and N K-edges are characteristics of honeycomb sp^2-bonding BN networks. The C K-edge, though being weaker, also show discernible π^* peak as well as δ^* band, indicating that C atoms are in the same sp^2-hybridized state as their BN counterparts and have been successfully incorporated into the BN lattice. The extracted atomic C/B+C+N ratios were 8% for B-C-N nanosheets. Because different B-C-N nanosheets had different layers, and C doping only happened in the outmost sheets of host BN, the extent of C doping varied among B-C-N nanosheets with different layers (see Figure S2, Supporting Information). That is, thin sheets had high C doping concentration while thick sheets had low C concentration. Here it is worth noting that the heating-rate of the thermal degradation was a crucial factor that sensitively affected the substitutional C doping process of BN nanosheets. Actually, there was a subtle competition between the formation of C-islands on BN surfaces and the real substitutional incorporation of C dopants into BN lattice in the thermal degradation process, and we had carefully optimized the heating-rate so as to get a control over the subtle competition.[32] A well-controlled, slow-rate temperature increase (≈1–2 K min^{-1}) can result in the degradation-generated C species that were tiny enough and thus chemically active enough to be successfully doped into the host BN lattice. On the other hand, when the heating-rate was increased (such as 10 K min^{-1}), much larger C fragments were generated which were hardly incorporated into the BN lattice and may form C-islands on BN surfaces. In our previous work, the substitution of C for B and N atoms in the BN honeycomb lattice had been demonstrated through spatially resolved EELS analyses and electrical measurements. Substitutional C doping transformed BN nanotubes from electrical insulators to semiconductors, inferring that the synthetic method used in our present work was reliable for incorporating C dopants into BN lattice.[32] In addition, this synthetic method had been developed by Wei et al. and they incorporated C atoms of organic molecules into the lattice of BN nanotubes[36] and BN nanosheets[37] via in situ electron-beam irradiation of the functionalized nanotubes or nanosheets in a TEM. Furthermore, Krivanek et al. had clearly distinguished individual C atom, that bonded with B and N atoms, in BN lattice using annular dark-field electron microscopy.[35] These works proved that the formation of substitutionally C-doped BN nanosheets through the random substitution of B and/or N atoms with separated C atoms was possible and feasible. In our present study, Crucial evidence for the substitutional incorporation of C dopants into the lattice of the BN nanosheets was provided by the X-ray photoelectron spectroscopy (XPS, Figure 1j and Figure S3, Supporting Information). As shown in Figure 1j, from the curve-fitted XPS spectra of C 1s core-level electrons, the existence of a significant amount of B-C and C-N bonds which rival that of the C-C bonds can be clearly identified, suggesting that the constituent B, C, and N elements have a real ternary bonding nature within the honeycomb lattice. It should be mentioned here that no magnetic impurities was detected by EELS and XPS in the B-C-N nanosheets. Nonetheless, we employed inductively coupled plasma-mass spectrometry (ICP-MS) to crosscheck this result, and found no d or f impurities above a detection limit of 10 ppm.

Static magnetization had been fruitfully exploited to probe the magnetic response of B-C-N nanosheets. Since the orientation of the B-C-N nanosheets in our samples was random, the detected magnetization signals of the samples were an average of B-C-N nanosheets over all possible orientations, and we didn't observe a difference in the response for different orientations of applied magnetic field H. **Figure 2**a shows the Zero-field-cooled (ZFC) and field-cooled (FC) temperature dependent magnetization (M-T) curves of the BN powders and B-C-N nanosheets in the temperature ranging from 5 to 300 K. Pristine, that is, undoped, BN powders were diamagnetic with a susceptibility of ≈ -5.5×10^{-7} e.m.u. g^{-1} Oe^{-1} (Figure 2a). With C doping, B-C-N nanosheets developed distinct ferromagnetic signal. The ferromagnetic behavior was also confirmed by isothermal magnetization versus applied magnetic field (M-H) measurements (Figure 2b,c). Ferromagnetic hysteresis from the B-C-N nanosheets was clearly apparent, with saturation of magnetization occurring at 8.87×10^{-3} e.m.u. g^{-1} and a coercivity of 145 Oe at 300 K, which was comparable to the reported behavior of defective HOPG.[8] The magnetization of

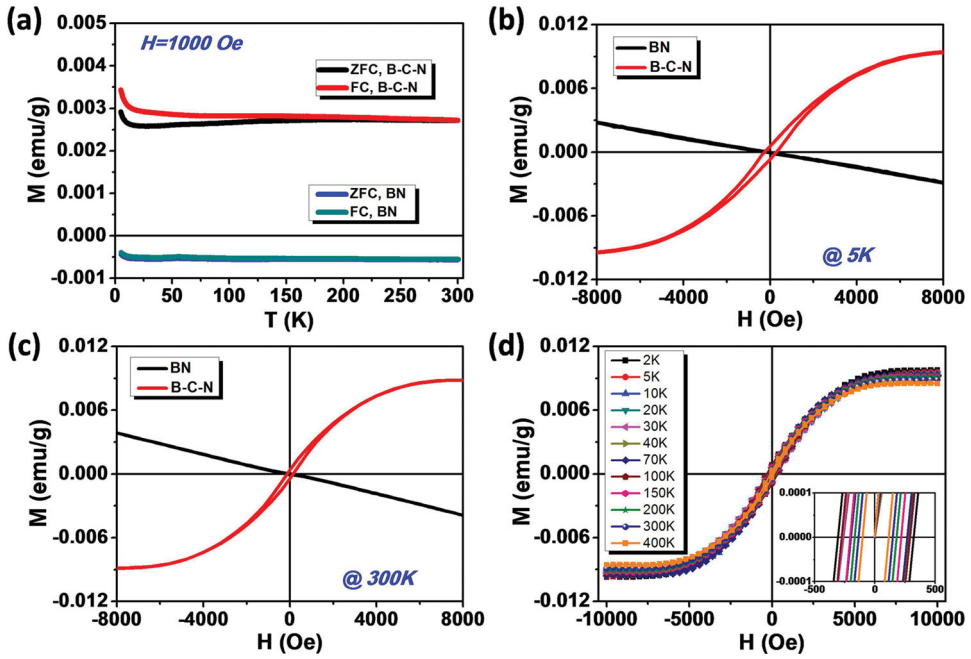

Figure 2. Ferromagnetism due to C doping. a) ZFC and FC temperature dependent magnetization curves of the B-C-N nanosheets and BN powders. b) Magnetization loops for B-C-N nanosheets at 5 K. c) Magnetization loops for B-C-N nanosheets at 300 K (the magnetization values were obtained after subtraction of a linear background contribution). d) Magnetization loops for B-C-N nanosheets measured at 2 to 400 K. Inset: Magnified loops for B-C-N nanosheets as shown in (d).

B-C-N nanosheets was practically temperature independent, at least up to 400 K (Figure 2d). Saturation magnetization values differed by less than 10% between 2 K and 400 K, indicating that the Curie temperature (T_c) of the B-C-N nanosheets must be higher than 400 K. After our initial discovery, we synthesized batch of samples and found this ferromagnetic behavior was repeatable and stable.

In addition to the magnetic response described, two other magnetic features imposed on the ferromagnetic signals of the B-C-N nanosheets had been observed. One was a small but finite paramagnetic upturn as the temperature decreased to 15 K (Figure 2a). A paramagnetic upturn at low temperature was also exhibited in C-based materials.[7,9,38,39] Sepioni et al. suggested that this behavior in graphene was related to a small number of unpassivated or unreconstructed point defects and zigzag edges.[7] The second was the divergence between the ZFC and FC curves starting around 250 K. Such magnetic anomaly was found when aitiferromagnetic correlations competed with ferromagnetic interactions. This result was similar to that obtained for graphene,[16,40,41] somewhat like spin glass behavior in frustrated system. Though the origin remained unclear, a coexistence of ferromagnetism and antiferromagnetism was well accepted for a biparticle system.[42] These two magnetic features were also detected in diamagnetic background of BN powders but somewhat weaker than those in B-C-N nanosheets. As pointed out above, point defects may affect the magnetic properties of BN, and it was plausible that in the process of C doping a number of defects were created (due to long time sonication), thus the contribution of defects to ferromagnetism observed in B-C-N nanosheets should be carefully taken into account. However, it was hard to estimate the contribution of defects to magnetism in B-C-N nanosheets directly. Since PTAS functionalized BN nanosheets had the same sonication process as the B-C-N nanosheets, the number of point defects between them was speculated to be on the same order, and we had measured the magnetic properties of the former. The magnetization of PTAS functionalized BN nanosheets was enhanced in comparison with BN powders (Figure S4, Supporting Information); however, they were still diamagnetic, indicating that the observed ferromagnetism was related to C doping rather than defects.

An important evidence we had against metal impurity effect was that neither BN powders nor PTAS functionalized BN nanosheets exhibited ferromagnetic signal (Figure 2 and Figure S4, Supporting Information). Furthermore, the measured content of magnetic metal impurities in B-C-N nanosheets was below 10 ppm, which was not sufficient to produce the ferromagnetic signal shown in Figure 2. These results excluded the possibility that the ferromagnetism of B-C-N samples was due to magnetic impurities. To confirm that C was the source of the ferromagnetism, an oxidation treatment was employed to remove C dopants in B-C-N nanosheets. It has been reported that B-C-N sheets can be efficiently transformed to BN sheets by an oxidation process at 923 K because C domains in the B-C-N sheets started to undergo oxidation in air at 823 K while oxidation of the BN layers in air began only at 1073 K.[43] An important result for us was that C dopants in B-C-N nanosheets could be eliminated selectively through an oxidation process at 923 K. One can find that burned in the O_2 atmosphere for 5 minutes, the B-C-N nanosheets were still ferromagnetic, while burning for 15 minutes can reduce the long-range magnetic order enormously (**Figure 3**a). As we increased the

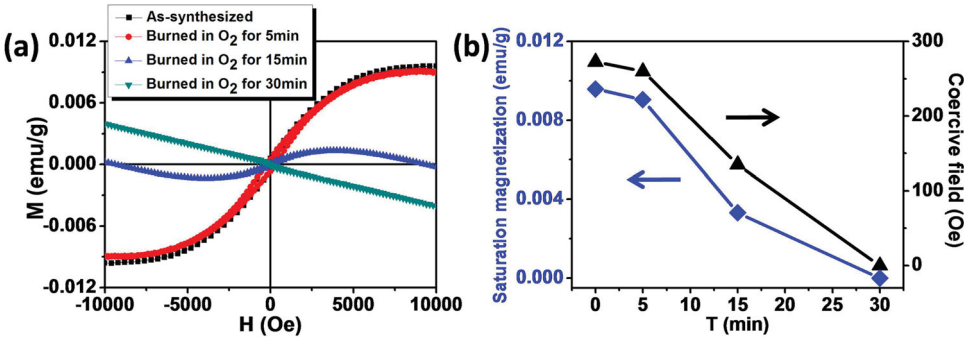

Figure 3. Effect of C elimination on ferromagnetism of B-C-N nanosheets. a) 5 K magnetization loops of as-synthesized B-C-N nanosheets and B-C-N nanosheets burned at 923 K in O_2 for 5 min, 15 min, and 30 min respectively. b) Saturation magnetization and coercive field corresponding to (a).

duration of burning in O_2 up to 30 minutes, the samples were turned from a ferromagnetic state to a diamagnetic state as that of pure BN. To gain further insight, Figure 3b plots the saturation magnetization and coercive field as a function of burning time. It was clear that saturation magnetization and coercive field gradually decreased with increasing the burning time. This evidence obviously proved that the ferromagnetism in B-C-N nanosheets merely originated from C doping: getting rid of C dopants could degrade magnetic moments, and could even destroy the ferromagnetic ordering completely.

As aforementioned, prior to our present experimental work, there have been some theoretical studies predicting that a C atom doping in a BN nantoube[29] or a 2D sheet[30] can induce spontaneous polarization. These theoretical studies gave a consistent picture that the C atom substitution for either B or N atom could form bonds with its three nearest neighbours, leaving one electron unpaired, and the spin polarization resulted from the unpaired electron of the C atom. We employed the SIESTA code[44] implementing first-principles calculations to reproduce this process. Our calculations for one C dopant doping in a BN supercell consisting of $4 \times 4 \times 1$ unit cells (Figure S5a, Supporting Information) confirmed that C substituting for either B or N atom resulted in an emergence of a flat band near the Fermi level, which split into two branches (Figure S5c,d, Supporting Information), leading to a spontaneous polarization with a local magnetic moment of 1.0 μ_B (Table S1, Supporting Information). The spin polarization was favoured by about 0.1 eV with respect to non-spin-polarized states in each case (Table S1, Supporting Information), which suggested that the spin polarization should be stable well above room temperature. To find out the origin of the spin polarization, we show the isosurface plot ($\rho = 1.2 \times 10^{-3}$ e/Å^3) of the spin polarization density (difference in densities of majority and minority spins) in real space for a C dopant substitution for a B atom (**Figure 4**a, the pictures were generated using the XCrySDen program.[45]) It was evident that the spin polarization density was localized around the C dopant and originated from it. This strong localization of the C dopant states leaded to the spin polarized ground state. Spontaneous polarization occurred when the relative gain in exchange interaction was larger than the penalty in kinetic energy.[42] As the flat band induced high density of localized electronic states around Fermi level, the penalty in kinetic energy would be infinitely small. Thus the flat band underwent spin polarization at any electron-electron repulsion and leaded to the formation of local magnetic moment in B-C-N system. These results were qualitatively the same as the flat band magnetism obtained in zigzag graphene nanoribbons[13,17] and C/BN heterostructures.[24,26]

Of course, existence of local magnetic moments did not necessarily lead to collective magnetism, which resulted from magnetic moments coupling. It was found that vacancy defect states in BN were far more extended than the strongly localized 3d or 4f electrons of magnetic ions.[22] Figure 4b clearly shows the extension of the C dopant states in BN. This duality of the C dopant states, which was also observed in nitrophenyl functionalized graphene,[46] opened up the possibility of long range magnetic couplings in the B-C-N system. To simulate the couplings between different magnetic moments, we doubled the size of the supercell and two C dopants were put in the supercell. Our calculation referred to the situation of two C dopants distributed over the two sublattices, and to the situation when C dopants belonged to sublattice B (or N) only. In the first situation, two C dopants substituted one B atom and one N atom. According to the Lieb's theorem,[47] the total spin S of the bipartite lattice equaled to $|N_A - N_B|/2$, where $(N_A - N_B)$ was the sublattice imbalance of atom numbers in bipartite lattice. In this situation, Lieb's theorem predicted that the total magnetic moment would be zero. This result was confirmed by our

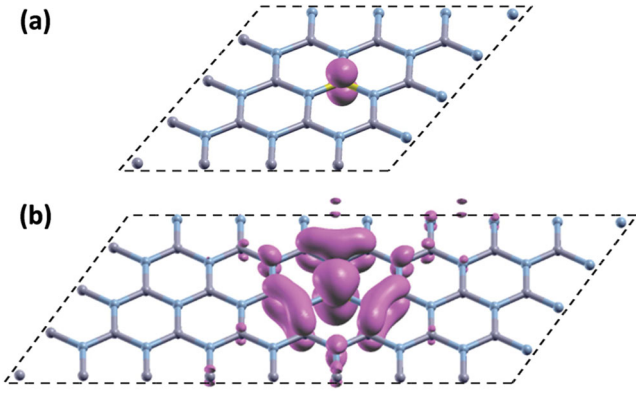

Figure 4. Isosurface charge density plot of the spin polarization states with a B atom substituted by a C dopant in (a) the supercell consisting of $4 \times 4 \times 1$ unit cells ($\rho = 1.2 \times 10^{-3}$ e/Å^3), showing the localized nature of C dopant states. b) Supercell consisting of $8 \times 4 \times 1$ unit cells ($\rho = 1.2 \times 10^{-4}$ e/ Å^3), showing both the localized nature and the extended tails of the C dopant states.

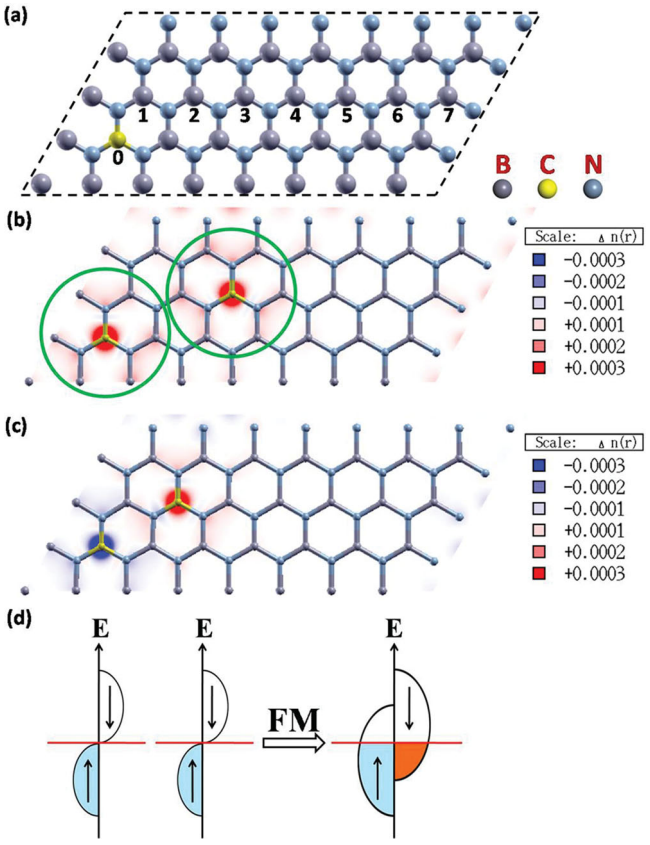

Figure 5. Theoretical analysis of the magnetism in B-C-N system. a) The ball-and-stick model of the $8 \times 4 \times 1$ supercell of B-C-N sheet. B atoms are indicated by grey balls, C atoms by yellow balls and N atoms by blue balls. b,c) Spatial distribution of the spin-polarization density ($n_{maj}(r) - n_{min}(r)$), where n_{maj} (n_{min}) is the charge density of the majority (minority) spin of the BN with two B atoms substituted by two C dopants (b) for B_0 and B_3 and (c) for B_0 and B_2. Unit: e/Å^3. d) Schematic illustration of the ferromagnetic coupling in the B-C-N system. The DOS in the majority and minority spin are plotted in blue and brown, respectively. The red line represents the Fermi level. The left side is the DOS for two isolated C dopants, and the right side denotes the final state after the ferromagnetic coupling for the B-C-N system.

theoretical results. For the second situation, when C dopants populated only B sublattice (**Figure 5**a, the first C dopant substituted B_0 and was fixed there, the second C dopant substituted B_7 to B_1 respectively), two stable magnetic structures were obtained: one was ferromagnetic, the other antiferromagnetic. In the ferromagnetic case (Figure 5b), most of the spin polarized states localized around the C dopants and leaded to the formation of local magnetic moment while the slowly decaying tail of the C dopant states (green circle) mediated the long-range magnetic coupling between the two moments. However, the total magnetic moment was partially suppressed and only 0.04 μ_B in this case. The departure from the expected value of 2 μ_B may because when C dopants were close, their interaction was strong and the coupling broadened the majority spin and the minority spin band widths, causing a charge transfer from the majority spin state to the minority spin state, thus reducing the magnetic moment (Figure 5d). The situation alternated as the distance between two C dopants decreased and the system would be more stable in the antiferromagnetic phase, due to the broaden of the dopant band equal to spin split, caused by the larger degree of overlap between the unpaired electrons (with a separation of about 0.44 nm, Figure 5c). The sensitivity of the exchange coupling to the distance between two magnetic moments had also been reported for defective C_{60}.[48] Our results indicated that the coupling between these C dopant induced local moments was fairly long-ranged with a moment separation of ≈0.6 nm. The exchange coupling between two local moments would vanish if the separation between defects was too long (the second C substituted $B_7 - B_4$). While the C dopant substituted B_1, because of the higher probability of formation of a covalent bond between the C dopants, the spin polarization disappeared. Our theoretical calculations above show that the spin moments induced by C doping can be (anti)ferromagnetically coupled to exhibit long-range magnetic ordering. The same results were calculated for N sublattice.

First principle calculations showed that the energy required for a C atom to substitute a B atom was lower than to substitute a N atom in BN system.[30,34] That is, more B atoms were substituted in the case of C doping. These results allowed us to conclude that the magnetic moment induced by C doants in sublattice B was larger than the one induced in sublattice N, thus playing a crucial role in producing ferromagnetism in system. Furthermore, we have quantitatively analyzed the magnetization signal to get the magnetic moment per C dopant. Different B-C-N samples had different layers and different C concentration. Since the most found C concentrations of our samples were that less than 10% (Figure 1i and Figure S2, Supporting Information), we choose the concentration of 5% to be the representative. With a C/B+C+N ratio of 5%, the number of C dopants per unit mass, was given by $N_C = (1/M_r)N_A \times 5\% = 1.21 \times 10^{21}$ dopants/g, where M_r was relative molecular weight of BN (24.82) and N_A was Avogadro's constant (6.02×10^{23}). The value of the 2 K saturation magnetization of B-C-N nanosheets was $M = 9.73 \times 10^{-3}$ emu g^{-1}, and, thus, the magnetic moment per C was given by $\mu_C = M/N_C \approx 8.04 \times 10^{-24}$ emu $\approx 8.67 \times 10^{-4}$ μ_B. Comparing with our theoretical value of 0.02 μ_B per C dopant, only one out of ≈25 C dopants seemed to contribute to the ferromagnetism in experiment. The first reason why the magnetic moment per C exhibited a lower value than the expected was that some C atoms formed islands on the surfaces of BN nanosheets rather than substituting B or N atoms in BN lattice. Apart from this reason, even for those C dopants substituting in BN lattice, the substitutional site (B or N) can also affect the total magnetic moment. As mentioned above, when two C dopants substituted one B atom and one N atom in a BN supercell, the total magnetic moment from these two C dopants was calculated to be zero. Therefore, only those C dopants (mainly at B site) that had no counterparts on the vicinal site sublattice would contribute to total magnetic moment. However, to what extent each factor will play a role is still a question that remains open to future theoretical and experimental studies in this field.

3. Conclusions

To conclude, the success in the synthesis of bulk-quantities of graphitic B-C-N nanosheets with high purity enabled us to

study the possible light-element magnetism in ternary B-C-N systems by means of bulk magnetization measurements. For the first time we observed the weak high-temperature ferromagnetism in such B-C-N based metal-free materials. Careful control experiments confirmed that the observed magnetic order should originate from the C dopants rather than from possible contamination of extrinsic magnetic impurities. These results represent substantial experimental support for the viability of previous theoretical predictions that the substitutional C doping of a honeycomb BN lattice can induce spontaneous spin polarization and lead to the formation of local magnetic moment. The occurrence of collective magnetism is then possible as a consequence of the (anti)ferromagnetic coupling between those local moments, as further revealed by DFT-based first-principles calculations in our present work.

4. Experimental Section

Materials: Commercially available BN powders (Wako Special Grade) were purchased from Wako Ltd.. HNO_3 (99.9999%) and NMP (HPLC Grade, 99.5%) were purchased from Alfa Aesar. PTAS was synthesized by following the procedures reported in ref. [32]. Extreme care was taken to use highest purity solvents (content of magnetic impurities <1 ppm) and also to avoid any contamination. Furthermore, in order to exclude the possible magnetic metal impurities, BN powders were thoroughly refluxed in diluted HNO_3 solution over night and then washed in ultrapure water, followed by annealing in NH_3 at 1373 K for 2 h.

Liquid Exfoliation of BN Powders: BN nanosheets were prepared by exfoliating BN particles in NMP, according to a published procedure.[33,49] Approximately, 500 mg of BN powders in 1000 ml NMP were sonicated in a low power sonic bath for 1 hour, resulting in milky white dispersions. The resultant dispersions received a mild centrifugation of 3000 rpm for 30 min. After centrifugation of the dispersions, the supernatant was decanted and was then filtered against a PTFE membrane (0.45 μm). The filter cake was dispersed in 50 ml ultrapure water with 30 min of sonication and filtered again. This process was repeated ten times and the final filter cake was redispersed in 300 ml ultrapure water (Figure 1b, upper left corner).

Synthesis of B-C-N Nanosheets: Similar to procedure used for synthesis of C doped BN nanotubes,[32] 300 mg of the PTAS were dispersed into BN nanosheets aqueous solution and the mixture was sonicated in a low power sonic bath for 10 h. The dispersions were filtered onto a PTFE membrane (0.2 μm), and we can get pink color powders (Figure 1b). Subsequently, the obtained powders were dried under vacuum at 373 K for 12 h. The dried powders were sealed into an evacuated ($<10^{-6}$ Torr) quartz ampoule with a diameter of ≈10 mm. Then the ampoule was heated to 1373 K in a muffle furnace with a controlled heating rate of 2 K min^{-1}, and isothermally held at this temperature for 2 h. After the ampoule cooled to room temperature, it was broken to take out the B-C-N samples. It can be shown that the original pink color of PTAS-BN nanosheets were changed to a grey color (Figure 1b) after this vacuum-annealing treatment process, which indicated the formation of the B-C-N nanosheets.

Structural Characterization and Magnetic Measurements: Transmission electron microscopy (TEM) imaging and electron energy loss spectroscopy (EELS) measurements were performed at 200 KV in a JEOL-2010F field-emission type high-resolution TEM equipped with a Gatan 666 parallel collection electron energy loss spectrometer. The microstructure and compositional analysis were studied by the Hitachi S4800 SEM machine with energy dispersive X-ray spectrum (EDX) facilities. XPS (Thermo Scientific Escalab 250) was carried out using monochromatic aluminum K X-rays. XPS data were analysed with the XPS-peak software. The magnetic impurity elements (such as Fe, Co, Ni or Mn) of all the samples are below 10 ppm measured by ICP spectrometry (ICP-MS, X Series 2, Thermo).The magnetization measurements were performed using a commercial SQUID-vibrating sample magnetometer (Quantum Design (QD) Inc., USA, model S-VSM). Because the magnetization signals of the samples were rather small we have checked the background signal from the sample holder in the VSM. The background signal was negligible in comparison with the sample response.

Computational Methods: All calculations were carried out within the SIESTA package,[44] using the Ceperley-Alder (CA) of local density approximation (LDA) for the exchange correlation energy. Single k-point and $20 \times 20 \times 1$ Monkhorst-Pack k-point grid were used in the structural optimizations and energy calculations, respectively. The energy convergence down to 10^{-4} hartree was guaranteed when the energy cutoff of 150 hartree was chosen in the energy calculations. A vacuum region of 39.9 Å was added along the direction normal to the sheet plane to avoid the interaction between periodic images of supercells. All the considered geometries were left to fully relax so that residual forces could become smaller than 0.01 eV/Å.

Supporting Information

Supporting Information is available from the Wiley Online Library or from the author.

Acknowledgements

The authors acknowledge financial support from the NSF (grant Nos. 21322304 and 11290161) and MOST (grant Nos. 2012CB933003 and 2013CB932603) of China.

Received: April 10, 2014
Revised: May 6, 2014
Published online: July 22, 2014

[1] P. Esquinazi, A. Setzer, R. Hohne, C. Semmelhack, Y. Kopelevich, D. Spemann, T. Butz, B. Kohlstrunk, M. Losche, *Phys. Rev. B* **2002**, *66*, 024429.
[2] P. Esquinazi, D. Spemann, R. Hohne, A. Setzer, K. H. Han, T. Butz, *Phys. Rev. Lett.* **2003**, *91*, 227201.
[3] K. H. Han, D. Spemann, P. Esquinazi, R. Hohne, V. Riede, T. Butz, *Adv. Mater.* **2003**, *15*, 1719.
[4] H. Pan, J. B. Yi, L. Shen, R. Q. Wu, J. H. Yang, J. Y. Lin, Y. P. Feng, J. Ding, L. H. Van, J. H. Yin, *Phys. Rev. Lett.* **2007**, *99*, 127201.
[5] R. D. Gunning, M. Venkatesan, D. H. Grayson, J. M. D. Coey, *Carbon* **2006**, *44*, 3213.
[6] B. Song, J. C. Han, J. K. Jian, H. Li, Y. C. Wang, H. Q. Bao, W. Y. Wang, H. B. Zuo, X. H. Zhang, S. H. Meng, X. L. Chen, *Phys. Rev. B* **2009**, *80*, 153203.
[7] M. Sepioni, R. R. Nair, S. Rablen, J. Narayanan, F. Tuna, R. Winpenny, A. K. Geim, I. V. Grigorieva, *Phys. Rev. Lett.* **2010**, *105*, 207205.
[8] J. Cervenka, M. I. Katsnelson, C. F. J. Flipse, *Nat. Phys.* **2009**, *5*, 840.
[9] R. R. Nair, M. Sepioni, I. L. Tsai, O. Lehtinen, J. Keinonen, A. V. Krasheninnikov, T. Thomson, A. K. Geim, I. V. Grigorieva, *Nat. Phys.* **2012**, *8*, 199.
[10] J. M. Hong, S. Niyogi, E. Bekyarova, M. E. Itkis, P. Ramesh, N. Amos, D. Litvinov, C. Berger, W. A. de Heer, S. Khizroev, R. C. Haddon, *Small* **2011**, *7*, 1175.
[11] J. M. Hong, E. Bekyarova, P. Liang, W. A. de Heer, R. C. Haddon, S. Khizroev, *Sci. Rep.* **2012**, *2*, 00624.
[12] Q. Feng, N. J. Tang, F. C. Liu, Q. Q. Cao, W. H. Zheng, W. C. Ren, X. G. Wan, Y. Du, *ACS Nano* **2013**, *7*, 6729.

[13] K. Tada, J. Haruyama, H. X. Yang, M. Chshiev, T. Matsui, H. Fukuyama, *Appl. Phys. Lett.* **2011**, *99*, 183111.
[14] D. M. Edwards, M. I. Katsnelson, *J. Phys.: Condens. Matter* **2006**, *18*, 7209.
[15] O. V. Yazyev, M. I. Katsnelson, *Phys. Rev. Lett.* **2008**, *100*, 047209.
[16] S. K. Saha, M. Baskey, D. Majumdar, *Adv. Mater.* **2010**, *22*, 5531.
[17] M. Fujita, K. Wakabayashi, K. Nakada, K. Kusakabe, *J. Phys. Soc. Jpn.* **1996**, *65*, 1920.
[18] Y. W. Son, M. L. Cohen, S. G. Louie, *Phys. Rev. Lett.* **2006**, *97*, 216803.
[19] R. F. Liu, C. Cheng, *Phys. Rev. B* **2007**, *76*, 014405.
[20] M. S. Si, D. S. Xue, *Phys. Rev. B* **2007**, *75*, 193409.
[21] J. Yang, D. Kim, J. Hong, X. H. Qian, *Surf. Sci.* **2010**, *604*, 1603.
[22] P. Dev, Y. Xue, P. H. Zhang, *Phys. Rev. Lett.* **2008**, *100*, 117204.
[23] S. Okada, A. Oshiyama, *Phys. Rev. Lett.* **2001**, *87*, 146803.
[24] J. Choi, Y. H. Kim, K. J. Chang, D. Tomanek, *Phys. Rev. B* **2003**, *67*, 125421.
[25] B. Huang, C. Si, H. Lee, L. Zhao, J. A. Wu, B. L. Gu, W. H. Duan, *Appl. Phys. Lett* **2010**, *97*, 043115.
[26] J. Nakamura, T. Nitta, A. Natori, *Phys. Rev. B* **2005**, *72*, 205429.
[27] J. M. Pruneda, *Phys. Rev. B* **2010**, *81*, 161409.
[28] A. Ramasubramaniam, D. Naveh, *Phys. Rev. B* **2011**, *84*, 075405.
[29] R. Q. Wu, L. Liu, G. W. Peng, Y. P. Feng, *Appl. Phys. Lett.* **2005**, *86*, 122510.
[30] R. Q. Wu, G. W. Peng, L. Liu, Y. P. Feng, *J. Phys.: Condens. Matter* **2006**, *18*, 569.
[31] B. Xu, Y. H. Lu, Y. P. Feng, J. Y. Lin, *J. Appl. Phys.* **2010**, *108*, 073711.
[32] W. L. Wang, Y. Bando, C. Y. Zhi, W. Y. Fu, E. G. Wang, D. Golberg, *J. Am. Chem. Soc.* **2008**, *130*, 8144.
[33] J. N. Coleman, M. Lotya, A. O'Neill, S. D. Bergin, P. J. King, U. Khan, K. Young, A. Gaucher, S. De, R. J. Smith, I. V. Shvets, S. K. Arora, G. Stanton, H. Y. Kim, K. Lee, G. T. Kim, G. S. Duesberg, T. Hallam, J. J. Boland, J. J. Wang, J. F. Donegan, J. C. Grunlan, G. Moriarty, A. Shmeliov, R. J. Nicholls, J. M. Perkins, E. M. Grieveson, K. Theuwissen, D. W. McComb, P. D. Nellist, V. Nicolosi, *Science* **2011**, *331*, 568.
[34] N. Berseneva, A. V. Krasheninnikov, R. M. Nieminen, *Phys. Rev. Lett.* **2011**, *107*, 035501.
[35] O. L. Krivanek, M. F. Chisholm, V. Nicolosi, T. J. Pennycook, G. J. Corbin, N. Dellby, M. F. Murfitt, C. S. Own, Z. S. Szilagyi, M. P. Oxley, S. T. Pantelides, S. J. Pennycook, *Nature* **2010**, *464*, 571.
[36] X. L. Wei, M. S. Wang, Y. Bando, D. Golberg, *J. Am. Chem. Soc.* **2010**, *132*, 13592.
[37] X. L. Wei, M. S. Wang, Y. Bando, D. Golberg, *ACS Nano* **2011**, *5*, 2916.
[38] X. L. Ding, H. Sun, X. M. Xie, H. C. Ren, F. Q. Huang, M. H. Jiang, *Phys. Rev. B* **2011**, *84*, 174417.
[39] V. Likodimos, S. Glenis, C. L. Lin, *Phys. Rev. B* **2005**, *72*, 045436.
[40] H. S. S. R. Matte, K. S. Subrahmanyam, C. N. R. Rao, *J. Phys. Chem. C* **2009**, *113*, 9982.
[41] L. L. Chen, L. W. Guo, Z. L. Li, H. Zhang, J. J. Lin, J. Huang, S. F. Jin, X. L. Chen, *Sci. Rep.* **2013**, *3*, 02599.
[42] O. V. Yazyev, *Rep. Prog. Phys.* **2010**, *73*, 056501.
[43] W. Q. Han, H. G. Yu, Z. X. Liu, *Appl. Phys. Lett.* **2011**, *98*, 203112.
[44] D. SanchezPortal, P. Ordejon, E. Artacho, J. M. Soler, *Int. J. Quantum Chem.* **1997**, *65*, 453.
[45] A. Kokalj, *Comp. Mater. Sci.* **2003**, *28*, 155.
[46] S. Niyogi, E. Bekyarova, J. Hong, S. Khizroev, C. Berger, W. de Heer, R. C. Haddon, *J. Phys. Chem. Lett.* **2011**, *2*, 2487.
[47] E. H. Lieb, *Phys. Rev. Lett.* **1989**, *62*, 1201.
[48] Y. H. Kim, J. Choi, K. J. Chang, D. Tomanek, *Phys. Rev. B* **2003**, *68*, 125420.
[49] X. Y. Zhang, A. C. Coleman, N. Katsonis, W. R. Browne, B. J. van Wees, B. L. Feringa, *Chem. Commun.* **2010**, *46*, 7539.